JACS
JOURNAL OF THE AMERICAN CHEMICAL SOCIETY

pubs.acs.org/JACS

Article

Measuring Nanometer Distances in Proteins and Rigid Rulers between ^{19}F and Gd^{3+} by Integration of ^{19}F-ENDOR Signal Intensities

Martyna Judd,* Mian Qi, Elwy H. Abdelkader, Haocheng Qianzhu, Anton Savitsky, Thomas Huber, Jeffrey R. Harmer, Adelheid Godt, Gottfried Otting, and Nicholas Cox*

Cite This: J. Am. Chem. Soc. 2025, 147, 16826−16835

Read Online

ACCESS | Metrics & More | Article Recommendations | Supporting Information

ABSTRACT: ^{19}F ENDOR is emerging as a powerful tool in structural biology for measuring distances in proteins labeled with ^{19}F and a paramagnetic tag. Due to spin−spin relaxation and line width limitations, it has been difficult to determine intertag distances larger than about 15 Å. Using a set of geometrically well-defined rulers and spin-labeled proteins, we show that ^{19}F−Gd^{3+} distances up to 20 Å can be accessed by integrating the intensity of the ENDOR spectrum, with distances approaching 30 Å potentially in reach as well. This method is robust when the intensities are scaled to a known reference, and provides scope for nanometer-scale triangulation of the coordinates of a ligand in a protein−ligand complex.

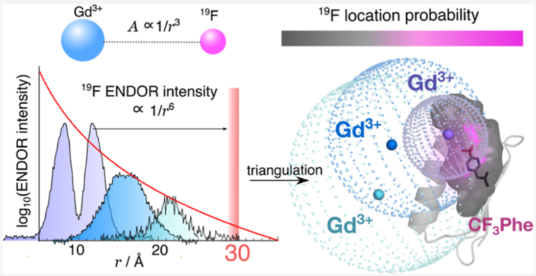

1. INTRODUCTION

Site-directed labeling with paramagnetic tags[1,2] is a well-established methodology for probing the three-dimensional structure of biomolecules by electron paramagnetic resonance (EPR) spectroscopy.[2−7] In particular, the dipolar interaction between two paramagnetic centers can be detected by double electron−electron resonance (DEER) experiments typically over a range of 20−80 Å,[8−17] allowing accurate distance determination. More recently, it has been shown that replacing one paramagnetic tag with a ^{19}F label allows shorter distances to be interrogated (5−20 Å) by using the electron−nuclear double resonance (ENDOR) experiment.[18−22] This technique exploits the hyperfine interaction between the electron spin and a ^{19}F nucleus, which manifests as a "splitting" of the ENDOR signal peak at the ^{19}F Larmor frequency. Like in DEER, distance determination by ENDOR relies on the $1/r^3$ distance dependence of the interspin dipolar coupling.

^{19}F ENDOR is attractive not only for its capacity to resolve distances up to 20 Å, but also because the ^{19}F atom can in principle substitute any hydrogen atom of a natural amino acid residue, meaning its position is constrained by the structure of the biomolecule. This is quite different from most cases of spin labeling with paramagnetic tags, which are attached to the protein surface by flexible tethers that have their own conformational distribution, largely independent of the flexibility and dynamics of the biomolecule. This results in the position of the paramagnetic center being described by a diffuse probability density, and therefore being much less well-defined than the position of the ^{19}F atom. On the other hand, using bacterial protein synthesis, the ^{19}F atom can be conveniently introduced with high fidelity and site-specificity by genetic encoding of a noncanonical ^{19}F-containing amino acid.[23−26]

In principle, paramagnetic relaxation enhancements (PRE) measured by solution nuclear magnetic resonance (NMR) spectroscopy can also measure distances in the 25−30 Å range, but this requires: (i) much more sample compared to EPR, (ii) an estimate of the effective rotational correlation time of the vector connecting the paramagnetic center with the nuclear spin, and (iii) complete reaction yields of the paramagnetic tag with the protein.[1] Furthermore, determining distance distributions from PRE data is not nearly as straightforward as from DEER. Extracting conformational information from ^{19}F-ENDOR is also challenging due to multiple line-broadening mechanisms.[27] ENDOR though, does have superior sensitivity compared to PRE, which opens the possibility of in-cell measurements at near-physiological concentrations.[28]

^{19}F ENDOR can also be performed with different spin tags, including organic radicals (nitroxide, trityl) or metal ions (Cu^{2+}, Gd^{3+}). It can provide interspin distance information as well as the ^{19}F chemical shift anisotropy (CSA) tensor in fixed molecular geometries.[21,29−31] We have previously demonstrated the advantages of using a Gd^{3+} ion as the paramagnetic tag to increase the sensitivity of ^{19}F ENDOR, allowing longer distances to be accessed than normally possible with nitroxide or trityl labels.[20] This result stems from a combination of the

Received: September 27, 2024
Revised: April 23, 2025
Accepted: April 23, 2025
Published: May 6, 2025

https://doi.org/10.1021/jacs.4c13530
J. Am. Chem. Soc. 2025, 147, 16826−16835

EPR properties of the Gd^{3+} ion, namely its high spin ($S = 7/2$), isotropic g-tensor, narrow central line, and favorable longitudinal relaxation time T_{1e}.

However, ^{19}F ENDOR currently still falls short of reliably covering the far end of the 5−20 Å distance range,[20,32] as the typical ENDOR line width of tens of kHz, limits the distance resolution to about 16 Å for an 18 kHz splitting.[20] Extending ^{19}F ENDOR to 20 Å and beyond is of particular interest for drug discovery, as longer-range ^{19}F ENDOR measurements would allow locating a ^{19}F-containing ligand bound to a protein that carries a paramagnetic label near the binding site.[33,34] In these kinds of measurements, being limited to short distances could result in perturbation of the drug-binding site if the spin tag is positioned too close. Longer distance measurements will also widen the scope of ENDOR to studies of protein dynamics in solution.[34] Furthermore, proteins already spin-labeled for DEER or NMR/PRE measurements[35] can be repurposed for ^{19}F ENDOR by using ^{19}F-labeled residues or ligands.

Recent literature has reported on different ways of overcoming the 16 Å distance ceiling of ENDOR measurements. The Goldfarb group has shown that using the higher order Gd^{3+} EPR transitions instead of the intense $|-1/2\rangle \leftrightarrow |+1/2\rangle$ transition allows smaller splittings to be resolved.[32] This method has been demonstrated for a 16 Å distance and has the potential to resolve up to ca. 20 Å distances, but does demand long accumulation times, approximately an order of magnitude longer than that for the $|-1/2\rangle \leftrightarrow |+1/2\rangle$ transition due to the broad spectral widths of the $|-5/2\rangle \leftrightarrow |-3/2\rangle$ and $|-7/2\rangle \leftrightarrow |-5/2\rangle$ transitions. Recent work by the Bennati lab has employed time domain (TD) ENDOR, which narrows the intrinsic ENDOR line width by eliminating power broadening from the RF pulse.[27] The remaining contribution to the line width was shown to arise from dipolar coupling of ^{19}F to nearby protons. Substitution of protons for deuterium in model compounds allowed line widths of 9 kHz to be achieved, setting the theoretical distance maximum to 20 Å.[27]

In the present work we examine an alternative and complementary approach for extending the distance range accessible to ^{19}F ENDOR at W-band (94 GHz) by using relative ENDOR signal intensities. The scope and limitations of this approach are described in detail.

2. RESULTS AND DISCUSSION

2.1. Theoretical ENDOR Distance Dependence. The intensity of the ENDOR signal is proportional to the power of the radiofrequency (RF) pulse excitation bandwidth, and the intrinsic ENDOR efficiency that depends on the electron−nuclear dipolar coupling strength. The latter contribution, termed F_{ENDOR},[36,37] is given by eq 1:

$$F_{\mathrm{ENDOR}} = \frac{1}{2}\sin^2\left(\frac{A}{2}\tau\right) \approx \frac{1}{2}\left(\frac{A}{2}\tau\right)^2 \propto \frac{1}{r^6} \tag{1}$$

where τ is the interpulse delay in the microwave detection sequence and A is the electron−nuclear hyperfine coupling, which can be assumed to be in the dipolar limit for sufficiently long distances r:

$$A = \frac{\mu_0}{4\pi\hbar}\frac{(g_e\beta_e g_n\beta_n)}{\boldsymbol{r}^3} \tag{2}$$

This leads to a $1/r^6$ dependence of the relative ENDOR intensity on the electron−nuclear distance,[37] which we demonstrated in previous preliminary experiments.[20] F_{ENDOR} can be equated to the integrated intensity of the ENDOR spectrum. The baseline of the ENDOR spectrum corresponds to the electron spin−echo intensity in the absence of a resonant RF excitation. Consequently, dividing the ENDOR intensity by the mean baseline value quantifies F_{ENDOR} as a percentage of the EPR echo intensity. To determine the distance from this integrated intensity, the F_{ENDOR} value of one spectrum can be normalized to that of a reference sample with a known distance corresponding to F_{REF}:

$$\frac{F_{\mathrm{ENDOR}}}{F_{\mathrm{REF}}} = \frac{r_{\mathrm{ref}}^6}{r^6} \tag{3}$$

Measuring ENDOR intensities accurately and reproducibly is considered difficult.[38−41] For eq 3 to work reliably, the target and reference samples must be measured under identical conditions, including solvent, sample concentration, and comparable spin label properties such as the electronic phase memory time T_M and nuclear longitudinal relaxation time T_{1n} (Supporting Information 5).

2.2. Rigid ^{19}F−Gd^{3+} Molecular Rulers. To test the reliability of this integration approach for distance determination, we first measured the set of rulers **1** (Figure 1A) with well-defined electron−nuclear distances between the Gd^{3+} ion and either ^{19}F (**1a**−**d**) or ^{13}C (**1e**). The ^{19}F−Gd^{3+} distances in the rulers **1a**−**d** are about 11.9, 14.3, 18.4, 20.8, respectively and the ^{13}C−Gd^{3+} distance is about 9.4 Å, as calculated from the contour lengths of the chemical structures. The distances were tailored by using *para*-phenylene (P) and ethyne (E) as the structural units for spacers between the spin label $[Gd(PyMTA)]^-$ and the ^{19}F or ^{13}C label. The contour lengths of the rulers **1** assume a cone of ^{19}F−Gd^{3+} vectors connecting the $[Gd(PyMTA)]^-$ group with the freely rotating CH_2CF_3 group.[20] Additional adjustments for the known bendability of the spacers[42,43] were not taken into account, as the spacers are quite stiff and the ruler lengths are short, resulting in negligible differences between the "real" ^{19}F−Gd^{3+} distances and the contour lengths.

The CF_3 group was chosen to achieve a greater ENDOR intensity compared to labeling with a single ^{19}F atom.[29] The CF_3 group was not directly bound to the benzene ring, but via a methylene linker, in order to exclude any through-bond coupling. This design choice followed from our previous work, where we measured the ENDOR spectrum of the conjugated ruler Gd-EPEP-F (structurally similar to **1d**) and determined a distance of about 10 Å rather than the designed 20 Å distance, raising suspicion of a through-bond coupling contribution.

However, further experiments suggested that this effect arises from solvent-driven aggregation of the ruler, addressed in the results below. In the present study all rulers were measured as 50 μM solutions in DMSO-d_6/10% glycerol-d_8 to minimize such aggregation-caused artifacts. All ENDOR experiments were performed at 10 K, exciting the central Gd^{3+} transition, where there are minimal contributions from higher order transitions to the overall ENDOR intensity (see Supporting Information 7).

Our experimental ENDOR results for rulers **1a**−**e** show very close agreement (within 0.4 Å) between the calculated contour lengths and the measured distances $\overline{r}_{\mathrm{int}}$ obtained from the integrated ^{19}F and ^{13}C ENDOR intensities (Table 1 and Figure 1B). The $\log_{10}(F_{\mathrm{ENDOR}})$ curve used for scaling the ^{19}F ENDOR data was calculated for the experimental interpulse delay

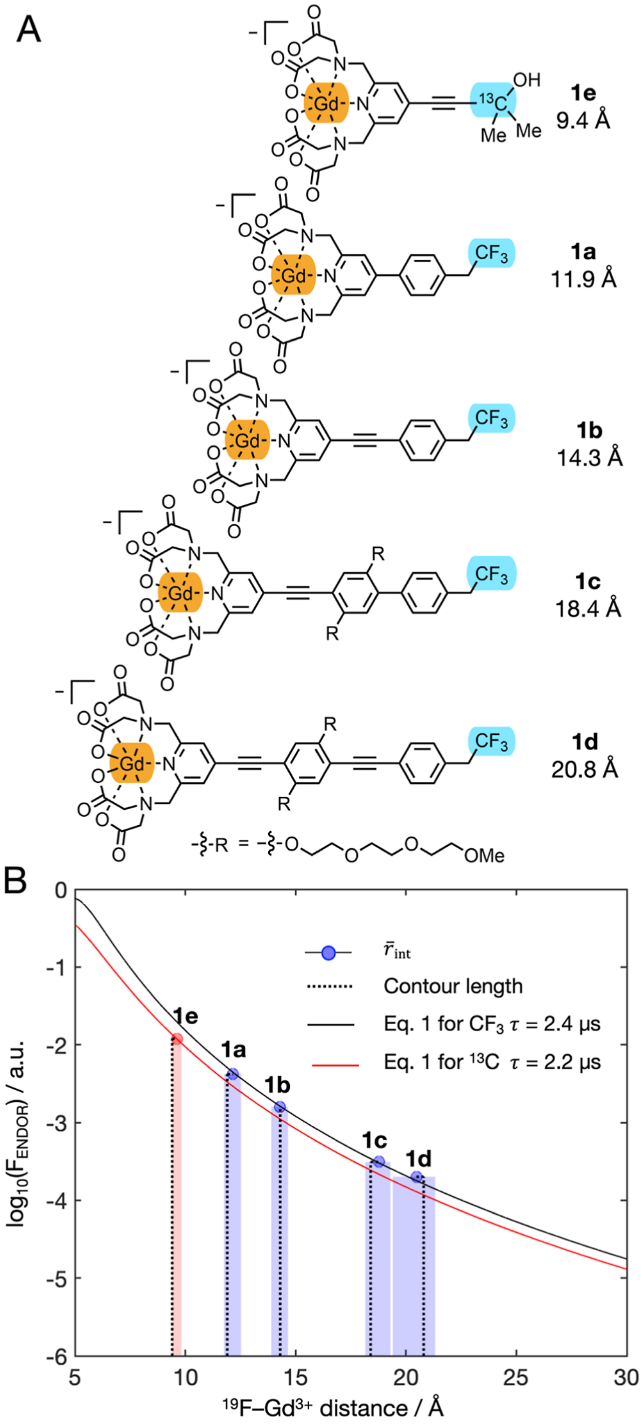

Figure 1. (A) Chemical structures of ^{19}F−Gd^{3+} rulers **1a**−**d** and ^{13}C−Gd^{3+} ruler **1e**. (B) Scaled experimental F_{ENDOR} intensities versus ^{19}F−Gd^{3+} and ^{13}C−Gd^{3+} distance. Predictions were made using eq 1, using $\tau = 2.4\ \mu s$ for ^{19}F measurements (black, solid curve) and $\tau = 2.2\ \mu s$ for ^{13}C measurements. The experimental points correspond to the distances $\overline{r}_{\text{int}}$ obtained by scaling with respect to the ^{19}F ENDOR intensity of ruler **1b**. The error ranges determined by propagating the experimental uncertainties (which primarily result from limited signal-to-noise ratios) are indicated by opaque bars.

parameter $\tau = 2.4\ \mu s$ (experimental Section 4.2), and the corresponding curve for the relative ^{13}C ENDOR intensity of **1e** was calculated for the experimental value $\tau = 2.2\ \mu s$. Ruler **1b** was used as the reference for ENDOR intensity scaling. Its ENDOR spectrum was fitted with a 25 ± 6 kHz dipolar coupling, consistent with the calculated contour length 14.3 Å distance (Supporting Information 3.2). This intermediate distance was chosen for the reference because the resolved splitting provides independent information on the distance, and the line shape is not affected by line-distorting blind-spotting associated with shorter distances.[18,19] In Table 1 we additionally provide the distances r_{read} that correspond to the dipolar couplings as visually read from the line splittings in the ENDOR spectra (Supporting Information 3.2). The distances $\overline{r}_{\text{ls}}$ in Table 1 are the distances predicted by modeling the experimental ENDOR line shape in EasySpin[46] (see Section 2.3). The corresponding uncertainties are estimated from (i) three times the resolution of the frequency axis in each spectrum[19,20] and (ii) covariance analysis (Supporting Information 2.2).

As seen from the shaded bars, which indicate the uncertainty ranges in Figure 1B, the uncertainties in the $\overline{r}_{\text{int}}$ distances increase, as expected, for the longer-distance rulers, which have lower ENDOR intensities and thus poorer SNR. The error bars were estimated by propagating relative integral uncertainties through eqs 1 and 3, considering the standard deviation of the noise vs the signal intensity (Supporting Information 2.1). It is worth noting that the uncertainty in $\overline{r}_{\text{int}}$ for short distances is comparable to the precision of the r_{read} and $\overline{r}_{\text{ls}}$ values determined from analysis of the ENDOR line shape. For distances ≳ 12 Å, where the dipolar splitting becomes on the order of the spectral line broadening, distances $\overline{r}_{\text{ls}}$ become much less precise than the mean distances $\overline{r}_{\text{int}}$ derived from the integrated ENDOR intensities.

Additional contributions to the uncertainties in $\overline{r}_{\text{int}}$ for rulers **1d** and **1e** stem from the need for background subtraction. Uncorrected measurements of **1d** underestimated the ^{19}F−Gd^{3+} distance by ∼2 Å from the expected trend predicted by the $\log_{10}(F_{\text{ENDOR}})$ curve, a finding we ascribe to the presence of aggregated molecules, which adds a significant background from short-range interspin interactions that obscures the low-intensity signal of the target 20.8 Å ^{19}F-Gd^{3+} distance (Supporting Information 3.1). The amount of aggregated molecules could be reduced to ca. 1.5% of the total population by using only DMSO-d_6 instead of the DMSO/10% glycerol-d_8 solvent mix. After performing a scaled subtraction of the aggregate spectrum (i.e., spectrum of **1d** in D_2O/10% glycerol-d_8 where the aggregation was most pronounced), from the spectrum of **1d** measured in DMSO-d_6, the now baseline-corrected integrated ENDOR intensity corresponds to a distance of 20.5 Å with an uncertainty range of −0.9/+1.5 Å, in full agreement with the contour-length distance of 20.8 Å (Figure 1B).

The data point of the ^{13}C−Gd^{3+} ruler **1e** (which has a ^{13}C−Gd^{3+} contour-length distance of 9.4 Å) can also be placed on the curve of the other rulers **1** at 9.6 + 0.5/−0.8 Å. This is done by scaling the measured ENDOR intensity by the factor $3[\gamma(^{19}\text{F})/\gamma(^{13}\text{C})]^2$ to account for the ratio of the ^{19}F and ^{13}C gyromagnetic ratios as well as the different number of spins. The raw ^{13}C ENDOR spectrum, however, is a superposition of both the expected 9.4 Å (25 kHz) ^{13}C−Gd^{3+} signal and a much larger background signal from the naturally occurring ^{13}C nuclei in the ruler structure. To isolate the ENDOR intensity of the ^{13}C label, we performed a scaled baseline subtraction using the natural abundance ^{13}C ENDOR spectrum of ruler **1b**, as described in Supporting Information 3.1. This, combined with the inherently lower sensitivity of ^{13}C

Table 1. Summary of Predicted ^{19}F−Gd^{3+}or ^{13}C−Gd^{3+} Distances of Rulers **1**[a]

			lineshape model		
ruler	contour length distance (Å)	$r_{read} \pm \sigma_r$ (Å)	$\overline{r}_{ls} \pm \sigma_r$ (Å)	lw ± σ (kHz)	integrated intensity $\overline{r}_{int} \pm \sigma_r$ (Å)
1a	11.9	11.4 + 0.5/−0.4	11.9 ± 0.1	34 ± 1.4	12.2 + 0.3/−0.4
1b	14.3	14.4 + 1.2/−0.7	14.3 ± 0.1	38 ± 1.0	ref +0.3/−0.4
1c	18.4	17.4 + 1.4/−1.1	17.0 ± 0.5	32 ± 2.0	18.8 + 0.5/−0.6
1d	20.8				20.5 + 0.9/−1.0
1e	9.4	9.3 ± 0.7			9.6 + 0.5/−0.8

[a] The lineshape model (Supporting Information 3.2) was used to simulate the experimental ENDOR spectra with resolved splittings using Easyspin *saffron* calculations in terms of (i) the mean ^{19}F−Gd^{3+}distance ($\overline{r}_{ls}$) and (ii) the ENDOR spectral line width (lw) assuming a Lorentzian lineshape convolution. Lineshape model uncertainties were calculated from covariance analysis of the fitted simulation parameters (Supporting Information 2.2). The integrated intensity uncertainties were calculated based on the SNR of the experimental data (Supporting Information 2.1). The r_{read} are the distances corresponding to the frequency splitting read off the spectrum using the dipolar coupling eq 2. The uncertainties are estimated by three times the frequency resolution in the x-axis of the spectrum.

ENDOR due to the F_{ENDOR} dependence on the nuclear gyromagnetic ratio (eq 1 and 2), significantly increases the uncertainty associated with this short-distance measurement.

2.3. Distances Determined from ENDOR Intensities in Spin-Labeled GB1 Proteins. We next examined a set of seven GB1 protein mutants (PDB: 1PGB)[44] labeled with the **Gd.C1** tag (a substituted [Gd(DOTAM)]$^{3+}$ tag)[45] and trifluoromethylphenylalanine (CF$_3$Phe). Samples were 50 μM solutions in deuterated buffer (50 mM MES in D$_2$O, pH 6.5, 50 mM NaCl) with 10% (v/v) glycerol-d_8. The expected ^{19}F−Gd^{3+} distances range between 8 Å and 30 Å according to the PDB crystal structure and chosen attachment sites (Figure 2). The Gd^{3+} ion is bound to the protein via the conformationally flexible tether of the **Gd.C1** tag, which introduces a ^{19}F−Gd^{3+} distance variation that is much larger than any orientational variation of the CF$_3$Phe residue (Supporting Information 4.2). As shown in ref 20, in this case the ^{19}F−Gd^{3+} distance can be reasonably described by a Gaussian distribution with a mean distance ($\overline{r}_{ls}$) and distribution width (δ_{ls}), which broadens the ENDOR spectrum, increasing the effective spectral line width (*lw*). We fitted these three parameters simultaneously via nonlinear least-squares optimization in MATLAB (convergence criteria of 10^{-6} for the standard deviation of the residuals of the experimental and fitted spectra), using the module *saffron* in EasySpin[46] to simulate the experimental ENDOR data, and refer to this as the line shape model. Additionally, we extended the error analysis of this model to calculate the covariances and 95% confidence intervals of the multiparameter fit (Supporting Information 2.2).

The best-fit parameters for the line shape models of proteins **2a**−**e**, whose spectra show resolved ^{19}F−Gd^{3+} dipolar splittings (Supporting Information 4.1), were used to benchmark the corresponding $\overline{r}_{int}$ distances. The fitted parameters are summarized in Figure 2C and Table 2. The red error bars in Figure 2C correspond to the 95% confidence intervals (σ_r) of the distances $\overline{r}_{ls}$ and indicate the quality of each fit. The best-fit distance distribution widths δ_{ls}, plotted as uncertainty ranges in black, describe the range of plausible ^{19}F−Gd^{3+} distances in the spin-labeled protein that could account for the experimental ENDOR line shape. As the ENDOR spectra of **2f** and **2g** did not resolve a splitting, rotamer simulations[47] were initially used to establish expected bounds on the ^{19}F−Gd^{3+} distances for these proteins. The black dotted error bars correspond to the full width at half-maximum (δ_{rot}) value of the rotamer-simulated ^{19}F−Gd^{3+} distance distributions. While rotamer libraries are a valuable tool for validating distance measurements in spin-labeled proteins,[20,47] they tend to overestimate the real distance range spanned by the spin labels, as they cannot accurately predict preferred conformations of the spin labels (Supporting Information 4.4 and ref 20). The distance bounds δ_{rot} shown in Figure 2C are therefore a conservative estimate of the plausible ^{19}F−Gd^{3+} distances in the protein **2f** and **2g.**

The experimental intensity-scaled ENDOR spectra of proteins **2** are shown in Figure 2B. Protein **2d** ($\overline{r}_{ls}$ = 16 ± 0.5 Å) was used as the reference for the integrated ENDOR intensity. Additionally, the $\overline{r}_{int}$ values for the short-distance proteins **2a** and **2b** were corrected for blindspotting artifacts with the help of EasySpin *saffron* calculations (Supporting Information 4.5). The performance of the $\overline{r}_{int}$ determination is summarized in the correlation plot of Figure 2C, which shows that the intensity-derived ^{19}F−Gd^{3+} distances are in very good agreement with the distances estimated from ENDOR line shape modeling and rotamer simulations. The uncertainty σ_r associated with $\overline{r}_{int}$ (blue error bars in Figure 2C) was estimated from the SNR, in the same way as for the rulers **1**, except that, for the protein data we additionally accounted for the uncertainty in the **2d** reference distance (Supporting Information 4.2). Consequently, the determined $\overline{r}_{int}$ distances of flexible proteins are inherently less precise compared to those of the rigid rulers **1**, where a higher precision reference distance, calculated from the contour length, is available.

For proteins **2a**−**e** the $\overline{r}_{int}$ and $\overline{r}_{ls}$ distances agree within about 0.3 Å (Figure 2C and Table 2). Compared to the results of the line shape model, the precision of $\overline{r}_{int}$ is predictably worse for the short-distance proteins **2a** and **2b**, but comparable for the intermediate-distance proteins **2c**−**e**. For the long-distance proteins **2f** and **2g** $\overline{r}_{int}$ is 20.5 ± 0.7 Å and 31.3 ± 3.4 Å, respectively. These distances fall well within the distance ranges predicted by rotamer simulations (18 Å (δ_{rot} = 4.1 Å) for **2f** and 30.9 Å (δ_{rot} = 4.3 Å) for **2g**). To the best of our knowledge, these two measurements represent only the second example of distances >20 Å determined by ^{19}F ENDOR in proteins. The Bennati/Bode group also reported a distance of ≳20 Å in an RNA complex, although only a lower bound distance could be confidently constrained from the line shape analysis alone.[22] We hypothesize that coupling this analysis with signal integration as is done here, would allow both upper and lower distance bounds to be estimated.

The $\overline{r}_{int}$ of **2f** could be additionally verified by a constrained line shape model analysis. The ENDOR spectrum of **2f** cannot be reliably simulated in the same way as proteins **2a**−**e** as the simulation parameters ($\overline{r}_{ls}$,δ_{ls} and lw) become highly correlated when the spectral line width is broader than the dipolar

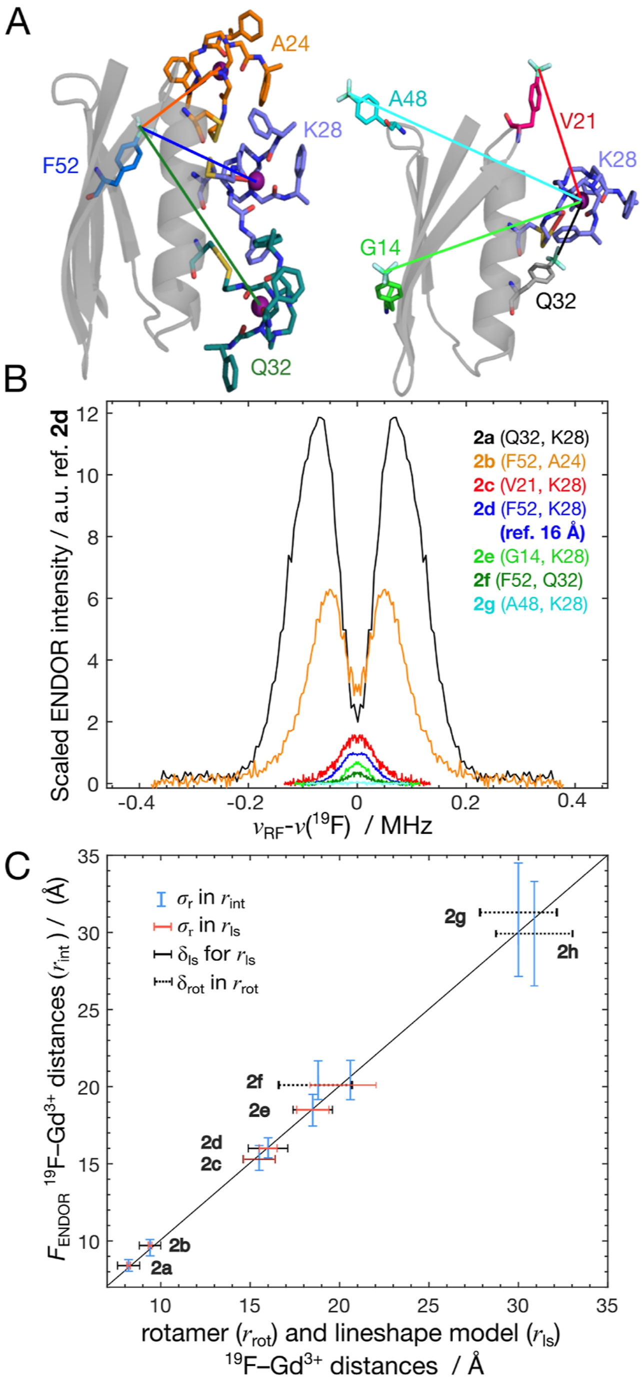

Figure 2. (A) Crystal structure of GB1 (PDB: 1PGB[44]), highlighting CF_3Phe mutation sites and locations of cysteine residues for **Gd.C1** attachment. (B) Experimental ^{19}F ENDOR data of proteins **2a**–**g**, symmetrized and scaled to the integrated ^{19}F ENDOR intensity of **2d** ($\overline{r}_{int}$ = 16 Å). (C) Correlation plot of distances $\overline{r}_{int}$ (blue lines) vs the distances $\overline{r}_{ls}$ and $\overline{r}_{rot}$ determined from either line shape modeling (red lines) or rotamer simulations (dotted black lines). For **2f** the line shape model was constrained using the lw and δ_{ls} fitted for **2a**–**e**. The intersection points compare the mean distances $\overline{r}$ determined by each method. The error bars indicate either the uncertainty (σ) in the $\overline{r}$ parameter or the width of the predicted distance distribution (δ), defining the range of viable distances.

coupling. However, the plausible parameter space of $\overline{r}_{ls}$ can be sampled by fixing lw and/or δ_{ls} to the values determined for the fits of **2a**–**e**. Using this "informed" line shape model we obtained $\overline{r}_{ls}$ values in the range 18.5–22.2 Å for **2f**, with a mean of $\overline{r}_{ls}$ = 20.6 Å. To further verify the distance of **2f** we performed preliminary ^{19}F ENDOR measurements using the higher order Gd(III) transitions as previously described by Bogdanov et al.[32] By measuring −33 mT off the central EPR transition at 4.8 K, we resolved a splitting of ~65 ± 6 kHz, corresponding to 20.1 + 0.5/−1 Å for the $7A_\perp$ splitting from the $|-7/2\rangle \leftrightarrow |-5/2\rangle$ transition (for full discussion see Supporting Information 7). Unfortunately, the SNR of the ENDOR spectrum of **2g** was too low to obtain a reasonable fit by a constrained line shape model or to measure the higher-order transition ENDOR spectrum. However, the convergence between the results of the different distance determination methods for the other proteins **2a**–**f** lends confidence to the $\overline{r}_{int}$ value derived for **2g**.

2.4. Enhancing Signal and Distance Sensitivity Using Labels with Higher Degree of Fluorination.

As with the long rulers **1c** and **1d**, the challenge with measuring long distances in the proteins **2f** and **2g** is the low SNR achievable, resulting in large uncertainty ranges in the distances predicted from ENDOR intensity scaling. To combat this, we investigated whether the ^{19}F signal intensity can be increased by using a fluorinated amino acid carrying more ^{19}F atoms. Protein **2h** is the same protein as **2g**, except with pentafluorosulfanylphenylalanine (SF_5Phe) instead of CF_3Phe. As expected, the ^{19}F ENDOR signal intensity scaled linearly: the SF_5Phe residue yielded an approximately 5/3 times larger signal (Figure 3). This SNR improvement reduced the integrated distance uncertainty from 31.3 (+4.2/−3.4) to 30.5 (+2.7/−2.8) Å, more confidently placing the lower limit for the distance at about 27.5 Å.

2.5. Spin Label Characteristics and Relaxation.

For accurate comparison with the measurements of the reference compound, it is important to keep the RF pulse parameters (Supporting Information 5.2), detection parameters and sample properties (solvent, concentration, homogeneity) identical to achieve reliable ENDOR intensity scaling. It is also necessary to use the same Gd^{3+} complex when calibrating integrated distances. This is because F_{ENDOR} is strongly dependent on the ratio of the electronic and nuclear spin–lattice relaxation dynamics (i.e., the T_{1e} and T_{1n} rates well as the cross relaxation T_{1x} rates).[48−50] For example, calibrating the set of protein distances by using one of the ruler complexes leads to a systematic increase in all estimated distances (see Supporting Information 5.1 for more details). We speculate that this may be due to differences in how the magnetization transfer is mediated between the Gd^{3+} and ^{19}F site in the proteins vs rulers, and may be reflected in the overall electronic and nuclear relaxation dynamics. Thus, a new calibration set is required for each Gd^{3+} spin tag/solvent regime. For more detail see Supporting Information 5.1.

Correctly interpreting ENDOR intensities also requires that the nucleus relaxes fully during the ENDOR experiment. Nuclear relaxation processes can be determined indirectly by measuring the ENDOR intensity as a function of the pulse sequence shot repetition rate (srt).[48] In an electron–nuclear coupled system, nuclei can either relax directly by single spin flip (T_{1n}) or by cross relaxation involving zero or double quantum transitions (T_{1x}), the latter generally being the faster process.[48] To confirm that the ENDOR intensities reflected nonsaturating conditions, we measured the ENDOR signals as a function of srt. We did not find an intensity or distance dependence of nuclear relaxation for either the rulers **1** nor the

Table 2. $^{19}F-Gd^{3+}$ Distances Predicted for Proteins 2[c]

			lineshape model			
protein	$\bar{r}_{rot}$ (δ_{rot}) (Å)	$r_{read} \pm \sigma_r$ (Å)	$\bar{r}_{ls} \pm \sigma_r$ (Å)	$\delta_{ls} \pm \sigma$ (Å)	$lw \pm \sigma$ (kHz)	integrated intensity $\bar{r}_{int} \pm \sigma_r$ (Å)
2a	6.9 (3.6)	7.8 + 0.2/−0.5	8.2 ± 0.1	1.2 ± 0.1	24 ± 3	8.4[a]+ 0.4/−0.4
2b	11.7 (3.6)	9.0 ± 0.3	9.4 ± 0.1	1.2 ± 0.1	25 ± 2	9.7[a]+ 0.4/−0.7
2c	17.2 (5.9)	17.0 + 1.3/−1.0	15.5 ± 0.9	1.8 ± 0.7	38 ± 6	15.3 + 0.9/−0.8
2d	14.5 (4.1)	15.5 + 0.8/−0.7	16.0 ± 0.5	2.2 ± 0.3	32 ± 6	**ref.** + 0.7/−0.6
2e	20.5 (5.1)	18.4 + 1.8/−1.3	18.5 ± 0.9	2.2 ± 0.8	25 ± 3	18.5 + 1.0/−1.1
2f	18.0 (4.1)		20.6 + 2.1/−1.6[b]	2.2 + 1.3/−1.1[b]		20.5 + 0.6/−0.7
2g	30.9 (4.3)					31.3 + 4.2/−3.4
2h						30.5 + 2.7/−2.8

[a]Blind-spot corrected intensity scaling using *saffron* simulations, see Supporting Information 4.3. [b]Lineshape model parameters for **2f** were determined using a constrained simulation as described in Section 2.3. [c]Lineshape model uncertainties were calculated from covariance analysis of the fitted simulation parameters, while the integrated intensity uncertainties were calculated based on the SNR of the experimental data. The rotamer simulation parameters are the mean distance ($\bar{r}_{rot}$) and distance distribution width (δ_{rot}) of the simulated $^{19}F-Gd^{3+}$ distributions plotted in the correlation plot Figure 2c, as well as a Lorentzian lineshape convolution (lw). The r_{read} are the distances corresponding to the frequency splitting read off the spectrum using the dipolar coupling eq 2. The uncertainties are estimated by three times the frequency resolution in the x-axis of the spectrum.

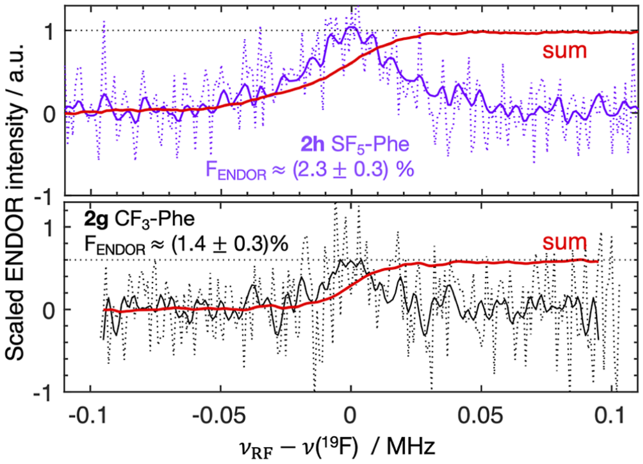

Figure 3. Experimental ^{19}F ENDOR spectra of proteins **2g** (black trace) and **2h** (purple trace) which report a distance of about 30 Å. The symmetrized and smoothed spectra (solid traces) are shown alongside the raw unsymmetrized data (dotted traces). Intensities are normalized to **2h** peak height, to highlight the ~5/3-fold signal increase using SF_5Phe instead of CF_3Phe. The red curves show the cumulative integral. The ENDOR efficiencies (F_{ENDOR}) and errors in F_{ENDOR} are annotated in the figure.

proteins **2a−e**, with distances of 8−18 Å (which had sufficient SNR to measure an srt dependence), indicating the measured intensities are robust (for further discussion see Supporting Information 5.3).

2.6. Triangulating Integrated Intensities to Locate the ^{19}F Spins and Gd^{3+} Spin Tag Position.

This work explored a potential protocol for using Gd^{3+} labeling and ^{19}F ENDOR distance measurements to determine small molecule binding to proteins. This would be of great interest in the study of membrane proteins, for which structure determination is difficult using other methods such as X-ray crystallography, NMR spectroscopy or cryo-electron microscopy. We show that by triangulating ENDOR-determined distances $\bar{r}_{int}$ for proteins labeled with a Gd^{3+} tag at different positions, the location of ^{19}F spins can be determined. For example, the proteins **2b**, **2d** and **2f** share the same CF_3Phe residue in position 52. Starting with the rotamer-generated Gd^{3+} coordinates for each **Gd.C1** tag site, we identified points on a sampling grid that are within a distance $\bar{r}_{int} \pm \sigma_{int}$ of the Gd^{3+} points, and used these to calculate the probability density for the CF_3 group in each protein. Multiplying the individual **2b**, **2d**, and **2e** probability densities, we obtained the triangulated probability density for the CF_3 group location within the protein. Figure 4 shows that the CF_3 location can be narrowed down to a region comprising the residues A23, Y45 and F52. Importantly, the high-probability (red) region of the triangulated surface overlaps with the crystal-structure position of the correct residue 52. The triangulated region of highest probability (Γ > 0.95) is 2.8 Å from the center of the CF_3 group of residue 52 in the GB1 crystal structure.

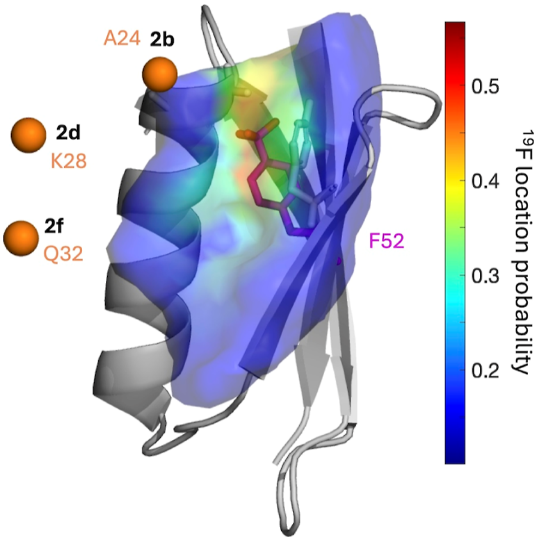

Figure 4. Triangulated probability density for locating the CF_3 group of the CF_3Phe residue determined by triangulating the ENDOR-determined distances in proteins **2b**, **2d** and **2f**. This triangulated surface encompasses three residues (shown in stick representations)—A23, Y45 and the native residue F52 (magenta). The region of highest probability (red, see color bar scale) encompasses the rotamer-predicted CF_3 coordinates. The mean Gd^{3+} ion locations determined from the rotamer-predicted probability densities of the **Gd.C1** labels are indicated by orange spheres.

The position of the Gd^{3+} ion of the **Gd.C1** tag can also be determined by triangulation using the ENDOR intensity data. Proteins **2a**, **2c**, **2d** and **2e** contain a CF_3Phe residue at

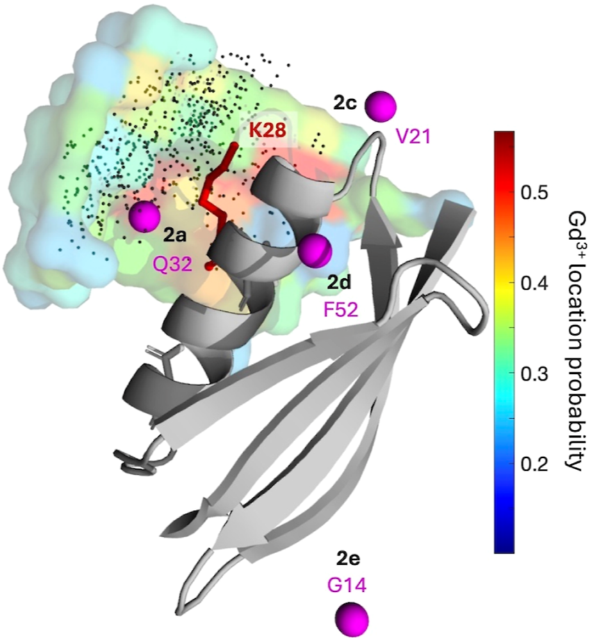

Figure 5. Triangulated probability density for locating **Gd.C1** tag position attached at position 28 (red stick representation) as determined from the integrated ENDOR intensities of proteins **2a**, **2c**, **2d** and **2e**. The color bar scaled probability volume of the Gd^{3+} ion is overlaid with the rotamer-predicted Gd^{3+} locations of the **Gd.C1** tag (black dots). The mean CF_3 coordinates predicted from the rotamer libraries of the CF_3Phe residues in the four proteins are indicated by magenta spheres.

different positions while sharing the **Gd.C1** position 28. Calculating the probability densities of the Gd^{3+} ion for these proteins using ^{19}F coordinates from individual CF_3Phe rotamer libraries as starting points, we identified sampling grid coordinates that fall within a distance $\overline{r}_{\text{int}} \pm \sigma_{\text{int}}$ of the ^{19}F points. At each grid point we additionally included a Gaussian distribution of width $\delta = 2$ Å to approximately account for flexibility in the tether of the **Gd.C1** tag. This process yielded a probability density surface for the Gd^{3+} ion, which is in very good agreement with the rotamer-predicted positions (Figure 5). In Supporting Information 6 we show that we can also map the probability surface for the likely **Gd.C1** attachment site by identifying residues with side chains within 10 Å (the **Gd.C1** tether length) of the triangulated Gd^{3+} coordinates. Only three residues (K28, V29, D36) fall within the 95% confidence interval of this probability volume, which includes the correct position 28.

A full workflow for the triangulation approach used to constrain the label positions is outlined in Supporting Information 6. Further development of triangulation and analysis approaches, particularly pertaining to distance distributions and uncertainty ranges, is the subject of ongoing research.

3. CONCLUSIONS AND OUTLOOK

^{19}F ENDOR intensities can be used to determine distances between 5 and 20 Å, with the potential to access up to 30 Å distances. For geometrically well-defined ruler complexes it provides sub-Ångstrom-level precision for distances up to 20 Å. While these measurements are, predictably, less precise in proteins labeled with flexibly attached spin tags, they nonetheless allow triangulating the position of the ^{19}F spin labels in a meaningful way. We envisage that measuring distances in this range could become routine for isolated proteins by using techniques and spin labels recently reported in the literature including: frequency-swept microwave pulses which can increase Mims ENDOR signals by a factor of 2,[51] Gd^{3+} complexes with short tethers,[35,52,53] deuterated spin labels, and Gd^{3+} complexes such as $[Gd(NO_3Pic)]$,[53−55] featuring an exceptionally narrow central EPR transition which will improve sensitivity. Such improvements may also allow longer distances to be measured in-cell and at submicromolar concentration up to about 30 Å. This distance is close to about half the thickness of biological membranes (typically 60−90 Å in thickness).[56] Thus, in experiments where Gd^{3+} spin labels can be introduced, we can envision using ^{19}F ENDOR to detect ^{19}F-labeled compounds binding to membrane proteins, without needing a priori knowledge of the ^{19}F location.

4. EXPERIMENTAL SECTION

4.1. Sample Preparation and Synthesis. Detailed information on the synthesis of rulers **1** is provided in Part II of the Supporting Information. The synthesis of proteins **2** was performed as described previously in ref 20 and further detailed information is also provided in Part II of the Supporting Information.

4.2. ENDOR Measurements. EPR and ENDOR experiments were performed on a 94 GHz (W-band) modified Bruker EPR spectrometer[57] equipped with a TE_{011}-mode EPR/ENDOR resonator in a helium gas flow cryostat (Oxford Instruments) operating at 10 K. All ^{19}F ENDOR and ^{13}C ENDOR spectra were acquired using the Mims ENDOR pulse sequence $\pi/2-\tau-\pi/2-t_{\pi,\text{RF}}-\pi/2-\tau-$echo, with $\pi/2 = 12$ ns. A relatively long τ value was chosen (2.4 μs for rulers **1** with longer electronic T_M times, and 2.0−2.2 μs for proteins **2**, which had shorter T_M times) to overcome blindspotting of the ENDOR line.[18−20] This value was substituted into the intensity-to-distance conversion from eq 1 to properly account for the impact of τ on the line shape and, hence, intensity of the ENDOR spectrum. For protein **2a**, significant blindspotting is observed in the ENDOR line shape. Therefore, this spectrum was acquired at several different τ values. Only the $\tau = 2.2$ μs spectrum was used for integrated intensity scaling, while for line shape model fitting, all spectra were simulated simultaneously and optimized to a unified parameter set.

All ^{19}F ENDOR measurements used a long RF pulse of 60 μs to avoid power-broadening of the ENDOR line.[19] The 100 W RF power source was attenuated by 3 dB to give the maximum ENDOR response for a 60 μs RF pulse length on the ^{19}F line for the rulers and short-distance proteins **2a−e**, and 6 dB for a 100 μs RF pulse length for long-distance proteins **2f** and **2g**. These power levels were determined by performing an RF nutation on both the proton line for calibration and on the ^{19}F line of protein **2b**, confirming that the ENDOR intensity remained constant and within the integration error in the 60−100 μs pulse length regime (see Supporting Information 5.1 for more detail) To acquire the ^{13}C spectra, a 40 μs RF pulse with 0 dB attenuation was used, similarly optimized using the RF nutation at the ^{13}C Larmor frequency. The ENDOR spectra were acquired in stochastic mode, with 1 shot per sample point and a 4 ms shot repetition time. Spectra of short-distance compounds (hyperfine coupling >20 kHz) were accumulated in 30−60 min per τ value (**1a**, **2a**, **2b**), 2−4 h (**2c**, **2d**, **2e**, **2f**), 6 h (**1b**, **1e**), 12 h (**1c**, **2h**), or 20−24 h (**1d**, **2g**). Where applicable, these recording times include the time taken to measure the spectrum used for background subtraction.

4.3. Simulations and Data Processing. All ENDOR data presented here are symmetrized, unless stated otherwise. To symmetrize the spectra, the center frequency was set to the nuclear Larmor frequency ν_N at the experimental field value, and the first half of the spectrum below ν_N was added to the second half above ν_N flipped. This approach improves the signal-to-noise without adding experimental averaging time. Importantly, at 94 GHz, in highly flexible (proteins **2**) or freely rotating groups (rulers **1**) we did not observe any asymmetries consistent with resolved chemical shift anisotropy, as expected, according to previous reports e.g. Kehl et al. in ref 29.

More details of the rotamer simulations and line shape model simulations of the ENDOR experimental data are provided in the Supporting Information and in ref 20. In brief, line shape simulations of the ENDOR spectra of the rulers **1** were performed using Mims ENDOR *saffron* calculations in EasySpin.[46] These were parametrized in terms of two variables: (i) the distance between the Gd^{3+} ion and the carbon atom of the CF_3 group (C_F), from which the tilt angle θ of the F_3 plane relative to the $Gd^{3+}-C_F$ vector is calculated to determine the mean $^{19}F-Gd^{3+}$ distance $\bar{r}_{ls}$; and (ii) the ENDOR spectral line width (lw) in kHz. Lineshape model simulations of the ENDOR spectra of proteins **2** were performed in terms of three variables: (i) the mean $^{19}F-Gd^{3+}$ distance $\bar{r}_{ls}$; (ii) the $^{19}F-Gd^{3+}$ distance distribution width δ_{ls} assuming a Gaussian distribution of the Gd^{3+} ion; and (iii) the ENDOR spectral line width (lw). The best-fit line shape model parameters for both rulers **1** and proteins **2** were determined using *fminsearch* in MATLAB. Uncertainties in the fitted parameters were analyzed using covariance analysis as outlined in Supporting Information 2.2. The conformation probability densities of CF_3Phe and Gd^{3+} of proteins **2** were additionally analyzed using rotamer simulations performed in PyParaTools as described in Supporting Information 4.2.

For distance determination using integrated ENDOR intensity scaling, each spectrum was divided by the mean baseline value, which corresponds to the EPR echo intensity in the absence of an RF pulse. The spectra were integrated to obtain relative intensity values, which were then substituted into eq 1. For the rulers **1**, ruler **1b** was used as the reference with the distance 14.3 Å obtained from the contour length calculation, and verified by line shape modeling of the experimental ^{19}F ENDOR spectrum. For proteins **2**, **2d** was used as the reference with the distance of 16 Å, similarly determined from the line shape model fit to the experimental ENDOR spectrum.

ASSOCIATED CONTENT

Supporting Information

The Supporting Information is available free of charge at https://pubs.acs.org/doi/10.1021/jacs.4c13530.

Supporting Information 1: Additional EPR measurements and data analysis for all compounds and proteins (PDF)

Supporting Information 2: Synthesis details for all compounds and proteins, and NMR and mass spec data for compounds **1a**−**e** (PDF)

AUTHOR INFORMATION

Corresponding Authors

Martyna Judd − *Research School of Chemistry, Australian National University, Canberra, Australian Capital Territory 2601, Australia*; Email: martyna.judd@anu.edu.au

Nicholas Cox − *Research School of Chemistry, Australian National University, Canberra, Australian Capital Territory 2601, Australia*; orcid.org/0000-0002-7815-6115; Email: nick.cox@anu.edu.au

Authors

Mian Qi − *Faculty of Chemistry and Center for Molecular Materials (CM2), Bielefeld University, Bielefeld 33615, Germany*

Elwy H. Abdelkader − *ARC Centre of Excellence for Innovations in Peptide & Protein Science, Research School of Chemistry, Australian National University, Canberra, Australian Capital Territory 2601, Australia*; orcid.org/0000-0002-5388-3949

Haocheng Qianzhu − *Research School of Chemistry, Australian National University, Canberra, Australian Capital Territory 2601, Australia*; orcid.org/0000-0002-7546-4411

Anton Savitsky − *Faculty of Physics, Technical University Dortmund, Dortmund 44227, Germany*

Thomas Huber − *Research School of Chemistry, Australian National University, Canberra, Australian Capital Territory 2601, Australia*; orcid.org/0000-0002-3680-8699

Jeffrey R. Harmer − *Centre for Advanced Imaging, Australian Institute for Bioengineering and Nanotechnology, The University of Queensland, St Lucia, QLD 4072, Australia*; orcid.org/0000-0003-4583-2401

Adelheid Godt − *Faculty of Chemistry and Center for Molecular Materials (CM2), Bielefeld University, Bielefeld 33615, Germany*; orcid.org/0000-0001-8453-1439

Gottfried Otting − *ARC Centre of Excellence for Innovations in Peptide & Protein Science, Research School of Chemistry, Australian National University, Canberra, Australian Capital Territory 2601, Australia*; orcid.org/0000-0002-0563-0146

Complete contact information is available at: https://pubs.acs.org/10.1021/jacs.4c13530

Notes

The authors declare no competing financial interest.

ACKNOWLEDGMENTS

We thank L. Stratmann, T. Dengel, and M. Hülsmann for their support with the ruler syntheses and J. Langley for help with edits to the final manuscript. Funding support by the Westpac Scholars Trust to M.J. is gratefully acknowledged. This work was funded by the Australian Research Council (grants CE200100012, DP210100088 and DP240100273).

REFERENCES

(1) Miao, Q.; Nitsche, C.; Orton, H.; Overhand, M.; Otting, G.; Ubbink, M. Paramagnetic chemical probes for studying biological macromolecules. *Chem. Rev.* **2022**, *122*, 9571−9642.

(2) Huang, K.; Fang, X. A review on recent advances in methods for site-directed spin labeling of long RNAs. *Int. J. Biol. Macromol.* **2023**, *239*, 124244.

(3) Li, H.; Pan, Y.; Yang, Z.; Rao, J.; Chen, B. Emerging applications of site-directed spin labeling electron paramagnetic resonance (SDSL-EPR) to study food protein structure, dynamics, and interaction. *Trends Food Sci. Technol.* **2021**, *109*, 37−50.

(4) Chavez, J. D.; Wippel, H. H.; Tang, X.; Keller, A.; Bruce, J. E. In-cell labeling and mass spectrometry for systems-level structural biology. *Chem. Rev.* **2022**, *122*, 7647−7689.

(5) Evans, R.; Ramisetty, S.; Kulkarni, P.; Weninger, K. Illuminating intrinsically disordered proteins with integrative structural biology. *Biomolecules* **2023**, *13*, 124.

(6) Singewald, K.; Hunter, H.; Cunningham, T. F.; Ruthstein, S.; Saxena, S. Measurement of protein dynamics from site directed Cu(II) labeling. *Analysis Sensing* **2023**, 3, No. e202200053.

(7) Roopnarine, O.; Thomas, D. D. Structural dynamics of protein interactions using site-directed spin labeling of cysteines to measure distances and rotational dynamics with EPR Spectroscopy. *Appl. Magn. Reson.* **2024**, *55*, 79−100.

(8) Milov, A. D.; Maryasov, A. G.; Tsvetkov, Y. D. Pulsed electron double resonance (PELDOR) and its applications in free-radicals research. *Appl. Magn. Reson.* **1998**, *15*, 107−143.

(9) Jeschke, G.; Chechik, V.; Ionita, P.; Godt, A.; Zimmermann, H.; Banham, J.; Timmel, C. R.; Hilger, D.; Jung, H. DeerAnalysis 2006 −

a comprehensive software package for analyzing pulsed ELDOR data. *Appl. Magn. Reson.* **2006**, *30*, 473−498.

(10) Schiemann, O.; Prisner, T. F. Long-range distance determinations in biomacromolecules by EPR spectroscopy. *Q. Rev. Biophys.* **2007**, *40*, 1−53.

(11) Borbat, P. P.; Georgieva, E. R.; Freed, J. H. Pros and cons of pulse dipolar ESR: DQC & DEER. *EPI Newsl.* **2007**, *17*, 21−33.

(12) Tsvetkov, Y. D.; Milov, A.; Maryasov, A. Pulse electron-electron double resonance (PELDOR) as nanometre range EPR spectroscopy. *Russ. Chem. Rev.* **2008**, *77*, 487.

(13) Potapov, A.; Yagi, H.; Huber, T.; Jergic, S.; Dixon, N. E.; Otting, G.; Goldfarb, D. Nanometer-scale distance measurements in proteins using Gd^{3+} spin labeling. *J. Am. Chem. Soc.* **2010**, *132*, 9040−9048.

(14) Jeschke, G. DEER distance measurements on proteins. *Annu. Rev. Phys. Chem.* **2012**, *63*, 419−446.

(15) Edwards, T. H.; Stoll, S. Optimal tikhonov regularization for DEER spectroscopy. *J. Magn. Reson.* **2018**, *288*, 58−68.

(16) Bahrenberg, T.; Yang, Y.; Goldfarb, D.; Feintuch, A. rDEER: A modified DEER sequence for distance measurements using shaped pulses. *Magnetochemistry* **2019**, *5*, 20.

(17) Schiemann, O.; Heubach, C. A.; Abdullin, D.; Ackermann, K.; Azarkh, M.; Bagryanskaya, E. G.; Drescher, M.; Endeward, B.; Freed, J. H.; Galazzo, L.; Goldfarb, D.; Hett, T.; Esteban Hofer, L.; Fábregas Ibáñez, L.; Hustedt, E. J.; Kucher, S.; Kuprov, I.; Lovett, J. E.; Meyer, A.; Ruthstein, S.; Saxena, S.; Stoll, S.; Timmel, C. R.; Di Valentin, M.; Mchaourab, H. S.; Prisner, T. F.; Bode, B. E.; Bordignon, E.; Bennati, M.; Jeschke, G. Benchmark test and guidelines for DEER/PELDOR experiments on nitroxide-labeled biomolecules. *J. Am. Chem. Soc.* **2021**, *143*, 17875−17890.

(18) Mims, W. B. Pulsed ENDOR experiments. *Proc. R. Soc. London, Ser. A* **1965**, *283*, 452−457.

(19) Meyer, A.; Dechert, S.; Dey, S.; Höbartner, C.; Bennati, M. Measurement of Angstrom to nanometer molecular distances with ^{19}F nuclear spins by EPR/ENDOR spectroscopy. *Angew. Chem., Int. Ed.* **2020**, *59*, 373−379.

(20) Judd, M. M.; Abdelkader, E. H.; Qi, M.; Harmer, J.; Huber, T.; Godt, A.; Savitsky, A.; Otting, G.; Cox, N. Short-range ENDOR distance measurements between Gd(III) and trifluoromethyl labels in proteins. *Phys. Chem. Chem. Phys.* **2022**, *24*, 25214−25226.

(21) Asanbaeva, N. B.; Sukhanov, A. A.; Diveikina, A. A.; Rogozhnikova, O. Y.; Trukhin, D. V.; Tormyshev, V. M.; Chubarov, A. S.; Maryasov, A. G.; Genaev, A. M.; Shernyukov, A. V.; Salnikov, G. E.; Lomzov, A. A.; Pyshnyi, D. V.; Bagryanskaya, E. G. Application of W-Band ^{19}F electron nuclear double resonance (ENDOR) spectroscopy to distance measurement using a trityl spin probe and a fluorine label. *Phys. Chem. Chem. Phys.* **2022**, *24*, 5982−6001.

(22) Remmel, L.; Meyer, A.; Ackermann, K.; Hagelueken, G.; Bennati, M.; Bode, B. E. Pulsed EPR methods in the Angstrom to nanometre scale shed light on the conformational flexibility of a fluoride riboswitch. *Angew. Chem., Int. Ed.* **2024**, *63*, No. e202411241.

(23) Qianzhu, H.; Abdelkader, E. H.; Otting, G.; Huber, T. Genetic encoding of fluoro-L-tryptophans for site-specific detection of conformational heterogeneity in proteins by NMR spectroscopy. *J. Am. Chem. Soc.* **2024**, *146*, 13641−13650.

(24) Qianzhu, H.; Abdelkader, E. H.; Herath, I. D.; Otting, G.; Huber, T. Site-specific incorporation of 7-fluoro-L-tryptophan into proteins by genetic encoding to monitor ligand binding by ^{19}F NMR spectroscopy. *ACS Sens.* **2022**, *7*, 44−49.

(25) Qianzhu, H.; Welegedara, A. P.; Williamson, H.; McGrath, A. E.; Mahawaththa, M. C.; Dixon, N. E.; Otting, G.; Huber, T. Genetic encoding of *para*-pentafluorosulfanyl phenylalanine: a highly hydrophobic and strongly electronegative group for stable protein interactions. *J. Am. Chem. Soc.* **2020**, *142*, 17277−17281.

(26) Jackson, J. C.; Hammill, J. T.; Mehl, R. A. Site-specific incorporation of a ^{19}F-amino acid into proteins as an NMR probe for characterizing protein structure and reactivity. *J. Am. Chem. Soc.* **2007**, *129*, 1160−1166.

(27) Kehl, A.; Sielaff, L.; Remmel, L.; Rämisch, M. L.; Bennati, M.; Meyer, A. Frequency and time domain ^{19}F ENDOR spectroscopy: role of nuclear dipolar couplings to determine distance distributions. *Phys. Chem. Chem. Phys.* **2025**, *27*, 1415−1425.

(28) Seal, M.; Zhu, W.; Dalaloyan, A.; Feintuch, A.; Bogdanov, A.; Frydman, V.; Su, X.-C.; Gronenborn, A. M.; Goldfarb, D. Gd^{III}-^{19}F distance measurements for proteins in cells by electron-nuclear double resonance. *Angew. Chem., Int. Ed.* **2023**, *62*, No. e202218780.

(29) Kehl, A.; Hiller, M.; Hecker, F.; Tkach, I.; Dechert, S.; Bennati, M.; Meyer, A. Resolution of chemical shift anisotropy in ^{19}F ENDOR spectroscopy at 263 GHz/9.4 T. *J. Magn. Reson.* **2021**, *333*, 107091.

(30) Schumann, S. L.; Kotnig, S.; Kutin, Y.; Drosou, M.; Stratmann, L. M.; Streltsova, Y.; Schnegg, A.; Pantazis, D. A.; Clever, G. H.; Kasanmascheff, M. Structure and flexibility of copper-modified DNA G-quadruplexes investigated by ^{19}F ENDOR experiments at 34 GHz. *Chem.—Eur. J.* **2023**, *29*, No. e202302527.

(31) Gauger, M.; Heinz, M.; Halbritter, A.-L. J.; Stelzl, L. S.; Erlenbach, N.; Hummer, G.; Sigurdsson, S. Th.; Prisner, T. Structure and internal dynamics of short RNA duplexes determined by a combination of pulsed EPR methods and MD simulations. *Angew. Chem., Int. Ed.* **2024**, *63*, No. e202402498.

(32) Bogdanov, A.; Frydman, V.; Seal, M.; Rapatskiy, L.; Schnegg, A.; Zhu, W.; Iron, M.; Gronenborn, A. M.; Goldfarb, D. Extending the range of distances accessible by ^{19}F electron−nuclear double resonance in proteins using high-spin Gd(III) labels. *J. Am. Chem. Soc.* **2024**, *146*, 6157−6167.

(33) Buchholz, C. R.; Pomerantz, W. C. K. ^{19}F NMR viewed through two different lenses: ligand-observed and protein-observed ^{19}F NMR applications for fragment-based drug discovery. *RSC Chem. Biol.* **2021**, *2*, 1312−1330.

(34) Kaczmarski, J. A.; Mahawaththa, M. C.; Feintuch, A.; Clifton, B. E.; Adams, L. A.; Goldfarb, D.; Otting, G.; Jackson, C. J. Altered conformational sampling along an evolutionary trajectory changes the catalytic activity of an enzyme. *Nat. Commun.* **2020**, *11*, 5945.

(35) Herath, I. D.; Breen, C.; Hewitt, S. H.; Berki, T. R.; Kassir, A. F.; Dodson, C.; Judd, M.; Jabar, S.; Cox, N.; Otting, G.; Butler, S. J. A Chiral lanthanide tag for stable and rigid attachment to single cysteine residues in proteins for NMR, EPR and time-resolved luminescence studies. *Chem.—Eur. J.* **2021**, *27*, 13009−13023.

(36) Gemperle, C.; Schweiger, A. Pulsed electron-nuclear double resonance methodology. *Chem. Rev.* **1991**, *91*, 1481−1505.

(37) Zänker, P.-P.; Jeschke, G.; Goldfarb, D. Distance measurements between paramagnetic centers and a planar object by matrix Mims electron nuclear double resonance. *J. Chem. Phys.* **2005**, *122*, 24515.

(38) Feher, G. Observation of nuclear magnetic resonances via the electron spin resonance line. *Phys. Rev.* **1956**, *103*, 834−835.

(39) Goldfarb, D.; Stoll, S. *EPR Spectroscopy: Fundamentals and Methods, eMagRes*; Wiley, 2018.

(40) Harmer, J. R. Hyperfine spectroscopy—ENDOR. In *eMagRes*; Harris, R. K., Wasylishen, R. L., Eds.; John Wiley & Sons, Ltd: Chichester, UK, 2016; pp 1493−1514.

(41) Pokern, Y.; Eltzner, B.; Huckemann, S. F.; Beeken, C.; Stubbe, J.; Tkach, I.; Bennati, M.; Hiller, M. Statistical analysis of ENDOR spectra. *Proc. Natl. Acad. Sci. U.S.A.* **2021**, *118*, No. e2023615118.

(42) Jeschke, G.; Sajid, M.; Schulte, M.; Ramezanian, N.; Volkov, A.; Zimmermann, H.; Godt, A. Flexibility of shape-persistent molecular building blocks composed of *p*-phenylene and ethynylene units. *J. Am. Chem. Soc.* **2010**, *132*, 10107−10117.

(43) Dalaloyan, A.; Qi, M.; Ruthstein, S.; Vega, S.; Godt, A.; Feintuch, A.; Goldfarb, D. Gd(III)-Gd(III) EPR distance measurements - the range of accessible distances and the iimpact of zero field splitting. *Phys. Chem. Chem. Phys.* **2015**, *17*, 18464−18476.

(44) Gallagher, T.; Alexander, P.; Bryan, P.; Gilliland, G. L. Two crystal structures of the B1 immunoglobulin-binding domain of streptococcal protein G and comparison with NMR. *Biochemistry* **1994**, *33*, 4721−4729.

(45) Graham, B.; Loh, C. T.; Swarbrick, J. D.; Ung, P.; Shin, J.; Yagi, H.; Jia, X.; Chhabra, S.; Barlow, N.; Pintacuda, G.; Huber, T.; Otting, G. DOTA-amide lanthanide tag for reliable generation of

pseudocontact shifts in protein NMR spectra. *Bioconjugate Chem.* **2011**, *22*, 2118−2125.

(46) Stoll, S.; Schweiger, A. EasySpin, a comprehensive software package for spectral simulation and analysis in EPR. *J. Magn. Reson.* **2006**, *178*, 42−55.

(47) Yagi, H.; Banerjee, D.; Graham, B.; Huber, T.; Goldfarb, D.; Otting, G. Gadolinium tagging for high-precision measurements of 6 nm distances in protein assemblies by EPR. *J. Am. Chem. Soc.* **2011**, *133*, 10418−10421.

(48) Epel, B.; Pöppl, A.; Manikandan, P.; Vega, S.; Goldfarb, D. The effect of spin relaxation on ENDOR spectra recorded at high magnetic fields and low temperatures. *J. Magn. Reson.* **2001**, *148*, 388−397.

(49) Stillman, A. E.; Schwartz, R. N. ENDOR Spin-echo spectroscopy. *Mol. Phys.* **1978**, *35*, 301−313.

(50) Bogdanov, A.; Gao, L.; Dalaloyan, A.; Zhu, W.; Seal, M.; Su, X.-C.; Frydman, V.; Liu, Y.; Gronenborn, A. M.; Goldfarb, D. Spin labels for ^{19}F ENDOR distance determination: resolution, sensitivity and distance predictability. *Phys. Chem. Chem. Phys.* **2024**, *26*, 26921−26932.

(51) Rogers, C. J.; Bogdanov, A.; Seal, M.; Thornton, M. E.; Su, X.-C.; Natrajan, L. S.; Goldfarb, D.; Bowen, A. M. Frequency swept pulses for the enhanced resolution of ENDOR spectra detecting on higher spin transitions of Gd(III). *J. Magn. Reson.* **2023**, *351*, 107447.

(52) Yang, Y.; Yang, F.; Gong, Y.-J.; Bahrenberg, T.; Feintuch, A.; Su, X.-C.; Goldfarb, D. High sensitivity in-cell EPR distance measurements on proteins using an optimized Gd(III) spin label. *J. Phys. Chem. Lett.* **2018**, *9*, 6119−6123.

(53) Shah, A.; Roux, A.; Starck, M.; Mosely, J. A.; Stevens, M.; Norman, D. G.; Hunter, R. I.; El Mkami, H.; Smith, G. M.; Parker, D.; Lovett, J. E. A Gadolinium spin label with both a narrow central transition and short tether for use in double electron electron resonance distance measurements. *Inorg. Chem.* **2019**, *58*, 3015−3025.

(54) Ossadnik, D.; Kuzin, S.; Qi, M.; Yulikov, M.; Godt, A. A Gd^{III}-based spin label at the limits for linewidth reduction through zero-field splitting optimization. *Inorg. Chem.* **2023**, *62*, 408−432.

(55) Borel, A.; Kang, H.; Gateau, C.; Mazzanti, M.; Clarkson, R. B.; Belford, R. L. Variable temperature and EPR frequency study of two aqueous Gd(III) complexes with unprecedented sharp lines. *J. Phys. Chem. A* **2006**, *110*, 12434−12438.

(56) Mitra, K.; Ubarretxena-Belandia, I.; Taguchi, T.; Warren, G.; Engelman, D. M. Modulation of the bilayer thickness of exocytic pathway membranes by membrane proteins rather than cholesterol. *Proc. Natl. Acad. Sci. U.S.A.* **2004**, *101*, 4083−4088.

(57) Nalepa, A.; Möbius, K.; Lubitz, W.; Savitsky, A. High-field ELDOR-detected NMR study of a nitroxide radical in disordered solids: towards characterization of heterogeneity of microenvironments in spin-labeled systems. *J. Magn. Reson.* **2014**, *242*, 203−213.